



Pronounced synergistic effect of the nano-sized PtSnNi/C catalyst for ethanol oxidation in direct ethanol fuel cell

Seden Beyhan^{a,b,*}, Jean-Michel Léger^b, Figen Kadirgan^a

^a Department of Chemistry, Faculty of Science and Letters, Istanbul Technical University, 34469 Maslak, Istanbul, Turkey

^b Electrocatalysis Group, IC2MP, UMR 7285, CNRS, Université de Poitiers, 40 avenue du Recteur Pineau, 86022 Poitiers Cedex, France

ARTICLE INFO

Article history:

Received 2 September 2012

Received in revised form 27 October 2012

Accepted 1 November 2012

Available online 22 November 2012

Keywords:

PtSnNi/C catalyst

PtSn-based catalyst

Ethanol oxidation

Direct ethanol fuel cell

ABSTRACT

Carbon supported well-dispersed Pt, Pt₉₀Sn₁₀, Pt₉₀Ni₁₀ and Pt₈₀Sn₁₀Ni₁₀ nanoparticles were synthesized by co-reduction using Bönnemann's colloidal precursor method. X-ray diffraction (XRD) analysis showed that catalysts have the Pt face centred cubic (fcc) structure and their crystallite size are in the range 2–6 nm. Regarding the ternary Pt₈₀Sn₁₀Ni₁₀/C catalyst, its lattice parameter is larger than that of Pt₉₀Ni₁₀/C and smaller than that of Pt₉₀Sn₁₀/C. The size of catalyst nanoparticles was observed via Transmission electron microscopy (TEM) and showed an average diameter of 3 nm. X-ray photon electron spectroscopy (XPS) results indicate that the surface of Pt₉₀Sn₁₀/C catalyst is enriched in Sn as compared to bulk composition, whereas Pt₈₀Sn₁₀Ni₁₀/C catalyst is Pt-enriched. The onset potentials for ethanol oxidation on Pt₉₀Sn₁₀/C and Pt₈₀Sn₁₀Ni₁₀/C catalysts were significantly lower than that of Pt/C and Pt₉₀Ni₁₀/C. Single direct ethanol fuel cell (DEFC) performances obtained for the Pt₈₀Sn₁₀Ni₁₀/C is promising when compared to that obtained with Pt₉₀Sn₁₀/C catalyst. The effect of Ni by promoting the C–C bond cleavage is confirmed by *in situ* IR measurements. These results suggest the presence of Ni in the Pt₈₀Sn₁₀Ni₁₀/C catalyst can facilitate C–C bond cleavage reaction on its Pt-rich surface; however, Sn oxide species activates the adsorbed CO on the surface providing the necessary OH species for oxidation of ethanol at lower potentials.

© 2012 Elsevier B.V. All rights reserved.

1. Introduction

Ethanol as a hydrogen-rich liquid for fuel cells is a very promising regarding its high power energy density, non toxicity, renewability and natural availability. For the commercialization aspects of direct ethanol fuel cell (DEFC), the design of an efficient anode catalyst should be a compromise between a high ability to break the C–C bond of the ethanol molecule at low over potential and a high tolerance to the partially oxidized products, especially CO and CH_x [1–4].

It has been reported that Pt–Sn catalyst shows the best catalytic performance for ethanol oxidation reaction (EOR) in the binary catalysts systems in acid media [5,6]. This is explained by the role of Sn in water dissociation at lower potentials than Pt. The adsorbed surface OH groups on Sn sites react with the adsorbed CO on Pt sites to form CO₂. Consequently, making alloys with Sn is a convenient way to modify the electrocatalytic properties of Pt in order to overcome poisoning due to the ethanol electrooxidation

intermediates, especially the adsorbed CO. However, the addition of Sn to Pt may inhibit the breaking the C–C bond, which is not favourable for ethanol energy conversion efficiency and fuel cell utilization. Therefore, much work has been done by adding the third elements to Pt–Sn binary catalyst to form PtSnRu [7–10], PtSnIr [11,12], PtSnIn [13], PtSnRh [14–18], PtSnNi [18–24], PtSnMo [25], PtSnW [26], PtSnEu [27], PtSnCe [28] and PtSnRe [29]. The beneficial effect of Ni addition to PtSn-based binary system has recently attracted the attention of some researchers, because of cost savings in a high catalytic performance and stability. However, the promoting mechanism of Ni to Pt–Sn is not fully developed yet.

Spinace et al. [19,20] studied the electro oxidation of ethanol and ethylene glycol on PtSn/C and PtSnNi/C catalysts prepared by alcohol reduction method. The superior performance and stability of the PtSnNi/C electrocatalyst was observed by chronoamperometry measurements at 0.5 V vs. RHE. They proposed that the modification of electronic properties of Pt in the presence of Ni oxides in PtSnNi/C catalysts, which may result in high performance towards ethanol oxidation. Bonesi et al. [21] was studied the influence of modification of carbon support on the catalytic activity of binary PtSn or ternary PtSnNi catalysts. They found that increasing number of oxygenated surface species on the modified carbon leads to a better EOR activity of PtSnNi than that of PtSn catalyst. Ribadeneira and Hoyos [22] claimed that the Ni addition

* Corresponding author at: Department of Chemistry, Faculty of Science and Letters, Istanbul Technical University, 34469 Maslak, Istanbul, Turkey.
Tel.: +90 212 285 72 70; fax: +90 212 285 63 86.

E-mail address: beyhanse@itu.edu.tr (S. Beyhan).

to Pt–Ru or Pt–Sn catalysts enhances the performance of DEFC. Almeida et al. [23] were synthesized at different composition of PtSnNi/C catalysts by thermal decomposition of polymeric precursor's method. In their study, $\text{Pt}_{83}\text{Sn}_{09}\text{Ni}_{08}/\text{C}$ and $\text{Pt}_{91}\text{Sn}_{06}\text{Ni}_{03}/\text{C}$ catalysts showed a high activity for ethanol oxidation at lower potential. During the electrolysis experiments, they performed high-performance liquid chromatography to analyze the reaction products. At high concentration of ethanol (1 M), they found that the only acetic acid and acetaldehyde was the reaction products without breaking the C–C bond of ethanol. Recently, dos Santos Correa et al. [24] studied the influence of the decrease of platinum and increase of the nickel content in the Pt–Sn–Ni catalyst using impregnation-reduction method. They found that the decrease in the Pt/Sn ratio is detrimental to improve the electrocatalytic activity for ethanol oxidation and proposed that the increase in Ni content enhances the catalytic activity of PtSn/C catalyst due to the simultaneous decrease in Pt/Sn ratio and increase in Ni content.

In the literature, catalysts synthesized with Bönnemann's colloidal precursor method showed a superior catalytic performance, durability and easy scale-up for practical applications in fuel cells [30–35]. On this basis, carbon-supported Pt, $\text{Pt}_{90}\text{Sn}_{10}$, $\text{Pt}_{90}\text{Ni}_{10}$ and $\text{Pt}_{80}\text{Sn}_{10}\text{Ni}_{10}$ nanoparticles were prepared by co-reduction using Bönnemann's method. To evaluate the relationship between the catalyst structure and catalytic performance, various physical techniques such as X-ray diffraction (XRD), Transmission electron microscopy (TEM), X-ray photon electron microscopy (XPS) and Energy dispersive X-ray (EDX) analysis were employed. The electrochemical EOR activity of $\text{Pt}_{80}\text{Sn}_{10}\text{Ni}_{10}/\text{C}$ catalyst was compared with its binary counterparts synthesized under the same experimental conditions. In situ infrared reflectance (IR) spectroscopy measurements allowed us to detect the product and by products of reaction. Single DEFC performance of the catalyst was tested as well.

2. Experimental

2.1. Preparation of electrocatalysts

Carbon supported Pt, $\text{Pt}_{90}\text{Sn}_{10}$, $\text{Pt}_{90}\text{Ni}_{10}$ and $\text{Pt}_{80}\text{Sn}_{10}\text{Ni}_{10}$ catalysts were prepared based on the procedure described by Bönnemann et al. [30–35]. But, this procedure was modified applying the single heat treatment step under nitrogen atmosphere at 300 °C for 1 h 30 h to generate activated carbon supported catalyst. All the metal salt reduction reactions were carried out under argon atmosphere, using non-hydrated metal chlorides salts and dry solvents. The catalyst ink was prepared by mixing twenty-five milligrams of carbon supported catalyst powder and 0.5 mL of Nafion® solution (5 wt.% from Aldrich) in 2.5 mL ultrapure water (Millipore MilliQ, 18 MΩ cm), which leads to a Nafion®/catalyst powder ratio close to 40 wt.%. 3 μL of ultrasonically homogenized ink was deposited from a micro syringe onto a freshly polished glassy carbon electrode yielding a total metal loading of 0.14 mg_{metal} cm⁻² before each experiments and the solvent was then evaporated in open air at room temperature.

2.2. Preparation of membrane electrode assemblies (MEAs)

To form a fuel cell anode electrode, the catalyst ink was prepared by mixing 100 μL of Nafion® (5 wt.% from Aldrich) solution, 1 mL of ethanol and 25 mg of catalytic powder. This mixture was then brushed on a carbon gas diffusion electrode in 5 cm² areas to give an approximate total metal loading of 2 mg cm⁻² on the anode. The gas diffusion layers (GDLs) were home-made using a carbon cloth (Electrochem Inc.) on which was brushed an ink made of Vulcan XC72 carbon powder and a PTFE/water emulsion (40% PTFE, 0.8 mg cm⁻²

Nafion®) in isopropanol yielding loading of a 4 mg cm⁻² mixture of carbon powder and 15 wt.% PTFE. The MEAs were prepared by hot pressing at 130 °C for 90 s under a pressure of 35 kg cm⁻², a pre-treated Nafion® 117 membrane with an E-TEK cathode (40% Pt/C with 2.0 mg cm⁻² Pt loading) and with the synthesized anodes catalysts.

2.3. Physical characterization of catalysts

2.3.1. X-ray diffraction (XRD)

X-ray diffraction patterns were collected by a Brucker D5005 diffractometer fitted with an AR monochromator and scintillation detector was used to determine catalysts structure and evaluate the particle size. The angle of the incident beam to the substrate surface was approximately 0.5°, and the detector was rotated to scan the samples. The 2θ angular region between 20° and 80° was explored at a scan rate of 0.1° s⁻¹ step. The Pt (220) peak was fitted well by Pearson 7 function using linear baseline correction for accurate measurements of full width at half maximum (fwhm) and peak position. The width of the Pt (220) peak was used to calculate the average crystallite size according to Scherer's equation [36]:

$$L = \frac{0.9\lambda_{\text{K}\alpha 1}}{\beta_{2\theta} \cos \theta_{\max}} \quad (1)$$

where L is the average crystallite size, θ_{\max} is the angle at the position of the peak maximum, $\beta_{2\theta}$ is the width of the peak (in radians) and $\lambda_{\text{K}\alpha 1}$ is the wavelength of X-rays used (1.54056 Å for Cu K $\alpha 1$ radiation). The lattice parameters of the catalysts were estimated according to Eq. (2) [36]:

$$a = \frac{\sqrt{2}\lambda_{\text{K}\alpha 1}}{\sin \theta_{\max}} \quad (2)$$

where a is the lattice parameter (nm) and all other symbols have same meanings as in Eq. (1).

2.3.2. X-ray photon electron spectroscopy (XPS)

Photoelectron spectra of selected catalysts were acquired with an ESCALAB 3 MKII de VG spectrometer equipped with a hemispherical electron analyzer and Mg K α ($h\nu = 1254.6$ eV) 300 W X-ray source. The spectra were collected at pass energy of 20 eV, which is typical of high-resolution conditions. The quantitative evaluation of each species was carried out by dividing the integrated peak area by empirical atomic sensitivity factors [37]. A background in spectral lines caused by in elastically scattered photoelectrons was removed using the well-known iterative integral method by Shirley [38] and fitting of the experimental curve to a combination of Lorentzian and Gaussian lines of variable proportions. All binding energies were determined by referencing to the C 1s peak at 284.9 eV.

2.3.3. Transmission electron microscopy (TEM)

The morphology, microstructure and elemental composition of catalysts were investigated by TEM and energy dispersive X-ray (EDX) analysis using a Philips CM 120 microscope/EDX analyzer equipped with a LaF₆ filament. The samples were prepared by adding a drop of the suspension, made by ultrasonically dispersing the catalyst in ethanol, onto a copper grid (200 meshes) covered with carbon film, and then evaporating the ethanol. Particle size and size distribution histogram of each sample was obtained by measuring more than 300 particles in the TEM images. The number average particle size d_{NA} is calculated using the following equation:

$$d_{NA} = \sum \frac{(i)n_id_i}{n} \quad (3)$$

where n_i is the frequency of the catalyst particles having diameter of size d_i and n is the total number of counted particles.

2.4. Electrochemical characterization

The electrochemical experiments were carried out in a conventional three-electrode cell at room temperature. Voltammetric curves using 0.1 M HClO₄ or 1 M EtOH/0.1 M HClO₄ electrolyte solutions purged with nitrogen gas were recorded with a Voltalab PGZ402. The solutions were prepared from HClO₄ 70% (Suprapur, Merck) in ultrapure water (MilliQ, Millipore 18 MΩ cm). The glassy carbon electrode was the working electrode (electrode area 0.071 cm²) on which the catalyst powder deposited. The counter electrode was a carbon plate and the reference electrode was a reversible hydrogen electrode (RHE).

2.5. Single cell tests

Fuel cell tests in a single cell with a 5 cm² geometric surface area were carried out with a Globe Tech test bench. The cell was fitted with MEA sandwich between two bipolar plates in channel-type flow bed. Ethanol solution (1 M and 2 M) was supplied by the liquid micro pump and O₂ was regulated by a flow metre. Back pressure valves allow controlling EtOH and oxygen pressure in the cell. Electrical heaters and a temperature controller were placed to heat the cell to the desired temperature. The fuel cell was operated for 30 min before each test to achieve steady-state polarization data, which was recorded using a high power potentiostat (Wenking model HP 88) interfaced with a PC to apply constant current sequences and to store the data, and a variable resistance in order to fix the current applied to the cell.

2.6. IR reflectance spectroscopy measurements

IR spectroscopy measurements were performed using a catalyst layer supported on a gold substrate (disk of 7 mm diameter) previously polished with alumina (0.5 μm) to a mirror-finish in order to obtain good reflectivity. The precursor solution was prepared by dispersing 25 mg of catalyst powder in a 2.5 mL of ultrapure water solution containing 0.5 mL 5% Nafion® via sonication for two hours. 8 μL of the resulting ink was then deposited onto the substrate by microsyringe and dried at room temperature. In situ IR reflectance spectra in the wavenumber region 1000–3000 cm⁻¹ were collected by a Fourier transform infrared spectrometer (Bruker IFS 66v) with an incidence angle of 65°. This instrument is equipped with nitrogen-cooled HgCdTe detector. The IR light beam passes entirely a chamber under vacuum before the observation of reflectance spectra of the electrode–electrolyte interface through the IR window (CaF₂) of a conventional thin layer spectroelectrochemical cell. This avoids recording parasitic spectra from the air atmosphere. Parallel polarized light was obtained from a BaF₂-supported Al grid polarizer. The cell potential was controlled using an LB 81 Wenking potentiostat and a Hi-tek waveform generator, connected to a BD 90 XY recorder. The spectral resolution was 4 cm⁻¹. The reproducibility of the spectral acquisition was controlled by repeating each experiment at least three times, with freshly prepared electrodes. Data acquisition and processing were performed using a computer with OPUS 5.5 software (developed by Bruker). To apply the technique of Single Potential Alteration Infrared Reflectance Spectroscopy (SPAIRS), the electrode reflectivity RE_i was regularly recorded each 0.05 V during the first cyclic voltammogram (CV) scan rate at 1 mV s⁻¹. This method is suitable for detecting the exact potential at which product is formed. Each spectrum resulted from the co-addition of 128 interferograms. The data acquisition required 50 s, i.e. over 0.05 V steps from 0.05 to 1 V vs. RHE increased the potential. The results were displayed as ΔR/R = (RE₂ - RE₁)/RE₁ = -ΔA, where RE₁ is the reflectivity at potential E₁ and RE₂ the reflectivity at the potential E₂. If E₁ < E₂, a

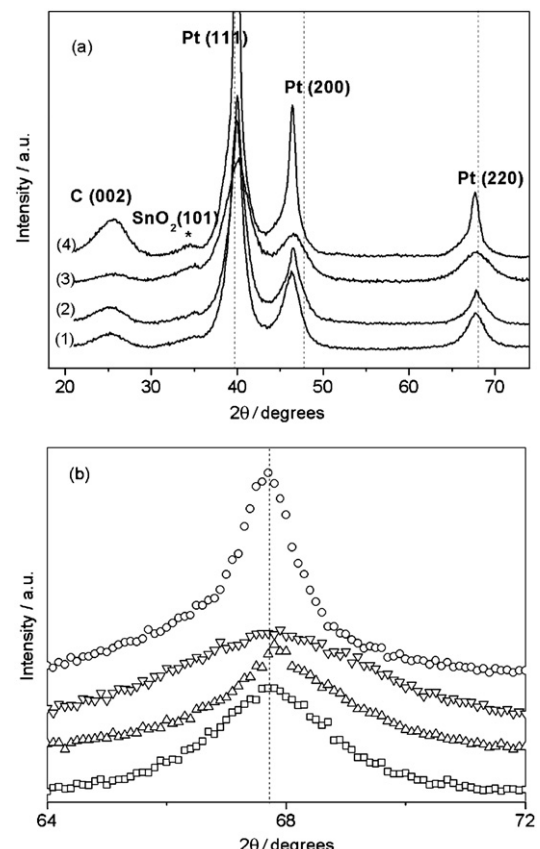


Fig. 1. (a) X-ray diffraction patterns of the Pt/C (1), Pt₉₀Ni₁₀/C (2), Pt₈₀Sn₁₀Ni₁₀/C (3) and Pt₉₀Sn₁₀/C catalysts (4), (b) an expanded view of the (220) reflections of the fcc phase.

positive absorption band indicates the consumption of species and a negative absorption band means the production of species.

3. Results and discussion

3.1. XRD analysis

X-ray diffraction patterns of Pt/C, Pt₉₀Sn₁₀/C, Pt₉₀Ni₁₀/C, Pt₈₀Sn₁₀Ni₁₀/C catalysts are given in Fig. 1a, together with the expanded view of the 220 diffraction peaks in Fig. 1b. The diffraction peak centred at 20–25° is attributed to Vulcan XC-72 carbon support whereas the other peaks are reflections of the fcc crystal lattice of Pt correspond to the planes (111), (200) and (220), respectively. For the Pt₉₀Sn₁₀/C catalyst, there is a small diffraction peak at around 34°, which could be indexed to the tetragonal structure of SnO₂ with the (101) plane (JCPDS File No. 41-1445). Also, the (110) diffraction peak of SnO₂ at around 27° overlaps with the (002) diffraction peak of carbon support, which probably induces the enhancement intensity of carbon support in the XRD patterns of Pt₉₀Sn₁₀/C catalysts as compared to the other catalysts. The lattice parameters and average crystallite size of catalysts obtained from XRD patterns are listed in Table 1. As can be seen from the results in Table 1, the lattice parameter of Pt/C catalyst ($a = 3.911 \text{ \AA}$) is smaller than that of the bulk Pt metal (JCPDS # 040802, $a = 3.923 \text{ \AA}$), owing to platinum–carbon interactions or depends on the particle size [39,40].

The diffraction peaks for the Pt₉₀Sn₁₀/C catalyst are slightly shifted to lower 2θ values with respect to the corresponding peaks for the Pt catalyst. Moreover, its lattice constant are 3.917 Å, between those of Pt₃Sn-ETEK (4.0015 Å) and Pt (3.911 Å).

Table 1

X-ray diffraction data analysis of Pt/C, Pt₉₀M₁₀ (M=Sn, Ni)/C and Pt₈₀Sn₁₀Ni₁₀/C catalysts.

Catalysts	Average crystallite size (nm) ^a	Lattice parameter (Å) ^b	(2 2 0) diffraction peak position (2θ°)
Pt/C	3.7	3.911	67.70
Pt ₉₀ Sn ₁₀ /C	6.1	3.917	67.58
Pt ₉₀ Ni ₁₀ /C	3.9	3.897	67.97
Pt ₈₀ Sn ₁₀ Ni ₁₀ /C	2.2	3.906	67.80

^a Calculated from Pearson7-fitted Pt (2 2 0) peak 2θ position according to Scherrer equation.

^b Calculated from Pearson7-fitted Pt (2 2 0) peak according to Bragg equation.

Table 2

Catalysts composition measured by EDX and XPS.

Nominal composition (at.%)	Bulk composition (EDX) (at.%)	Surface composition (XPS) (at.%)	(Sn/Pt) _{XPS}
Pt ₉₀ Sn ₁₀	Pt ₇₂ Sn ₂₈	Pt ₆₉ Sn ₃₁	0.45
Pt ₉₀ Ni ₁₀	Pt ₉₀ Ni ₁₀	n.d.	—
Pt ₈₀ Sn ₁₀ Ni ₁₀	Pt ₈₁ Sn ₁₁ Ni ₈	Pt ₈₄ Sn ₁₆	0.19

n.d.: not determined.

According to Kuznetzov et al. [41], Pt forms nearly all possible alloys with Sn, and the shift of the peaks to lower angles reveals this alloy formation between Pt and Sn, due to the incorporation of Sn in the fcc structure of Pt. Regarding the ternary Pt₈₀Sn₁₀Ni₁₀/C catalyst, its lattice parameter is larger than that of Pt₉₀Ni₁₀/C and smaller than that of Pt₉₀Sn₁₀/C (see Table 1). This intermediate value of the lattice parameter of the Pt₈₀Sn₁₀Ni₁₀/C catalyst indicates the partial substitution of Pt with Ni and Sn atoms, which can be introduced by shifting of the XRD peaks in opposite directions.

3.2. EDX and XPS analysis

EDX and XPS results without taking into account of the oxygen content are summarized in Table 2. It is found that the bulk elemental compositions of the Pt₉₀Ni₁₀/C and Pt₈₀Sn₁₀Ni₁₀/C catalysts are similar to the nominal ones, except for the Sn content in the Pt₉₀Sn₁₀/C catalyst which is three times higher than the expected value.

Determination of surface composition from the XPS results (see Table 2) indicate that the surfaces of the Pt₉₀Sn₁₀/C particle is enriched in Sn as compared to bulk composition, (Sn/Pt=0.45), whereas for Pt₈₀Sn₁₀Ni₁₀/C is Pt-enriched. Their surface is mostly composed of oxidized states of platinum and tin as revealed from the binding energy.

Table 3 shows the binding energies for Pt 4f_{7/2} level in Pt/C, Pt₉₀Sn₁₀/C and Pt₈₀Sn₁₀Ni₁₀/C and for Sn 3d_{5/2} level in Pt₉₀Sn₁₀/C

Table 3

XPS analysis of Pt/C, Pt₉₀Sn₁₀/C and Pt₈₀Sn₁₀Ni₁₀/C catalysts: binding energies (eV) and Pt/C surface atomic ratios.

Sample	BE (eV)		Pt/C (at.%)
	Pt 4f _{7/2} ^a	Sn 3d _{5/2} ^a	
Pt/C	72.26 (56) 73.22 (35) 74.79 (9)	—	0.056
Pt ₉₀ Sn ₁₀ /C	71.67 (3)	486.55 (13)	0.026
	72.10 (61)	487.88 (87)	
	73.21 (36)	—	
Pt ₈₀ Sn ₁₀ Ni ₁₀ /C	72.13 (33)	487.51	0.060
	72.93 (50)	—	
	74.81 (17)	—	

^a Values in parentheses indicate the relative percentage of surface species for each sample.

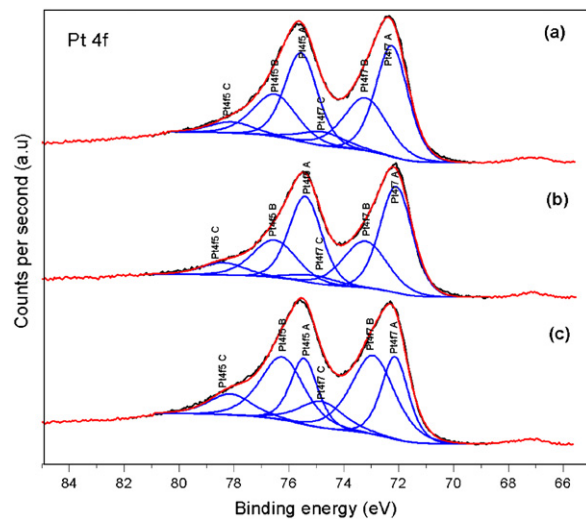


Fig. 2. XPS spectra of Pt 4f_{7/2} level for Pt/C (a), Pt₉₀Sn₁₀/C (b) and Pt₈₀Sn₁₀Ni₁₀/C (c) catalysts.

and Pt₈₀Sn₁₀Ni₁₀/C catalysts. The Pt 4f signal doublet is fitted to three components in all catalysts. The first 4f_{7/2} component with a low binding energy (BE) at 71.67–72.26 eV would attribute to metallic Pt. A second one observed at 72.10–73.22 eV could be assigned to Pt²⁺ species in PtO and Pt(OH)₂-like species and a third one appeared even higher BEs at 73.21–74.81 eV, corresponds to a higher oxidation state Pt⁴⁺. The relative amounts of Pt in each of these three states are shown in Table 3 as a percentage. Although the binding energies values of Pt 4f_{7/2} levels for three oxidation states are reported in the literature [42] as follows: Pt⁰: 71.0–71.3 eV, Pt²⁺: 72.8–73.4 eV and Pt⁴⁺: 74.1–74.3 eV, the observed binding energies are significantly higher than those reported (see Table 3). Noticeably, this shifting in Pt/C catalyst is higher than in the other catalyst may be due to a stronger interaction of the Pt species with support compared to the others. In any case, it seems that there were three different species: one with oxidation state close zero and the other two species close to (II) and (IV) oxidation state.

Table 3 also shows the values of dispersion of Pt on carbon support with surface atomic ratios in the range from 0.026 to 0.060. These values indicate that the lower dispersion in the Pt₉₀Sn₁₀/C catalyst compared to the others. Furthermore, a higher

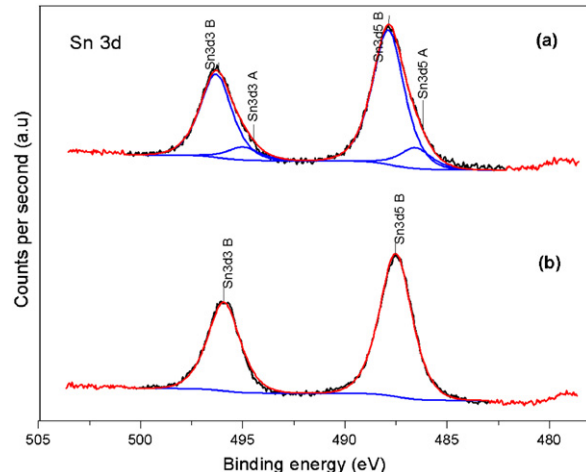


Fig. 3. XPS spectra of Sn 3d_{5/2} level for Pt₉₀Sn₁₀/C (a) and Pt₈₀Sn₁₀Ni₁₀/C (b) catalysts.

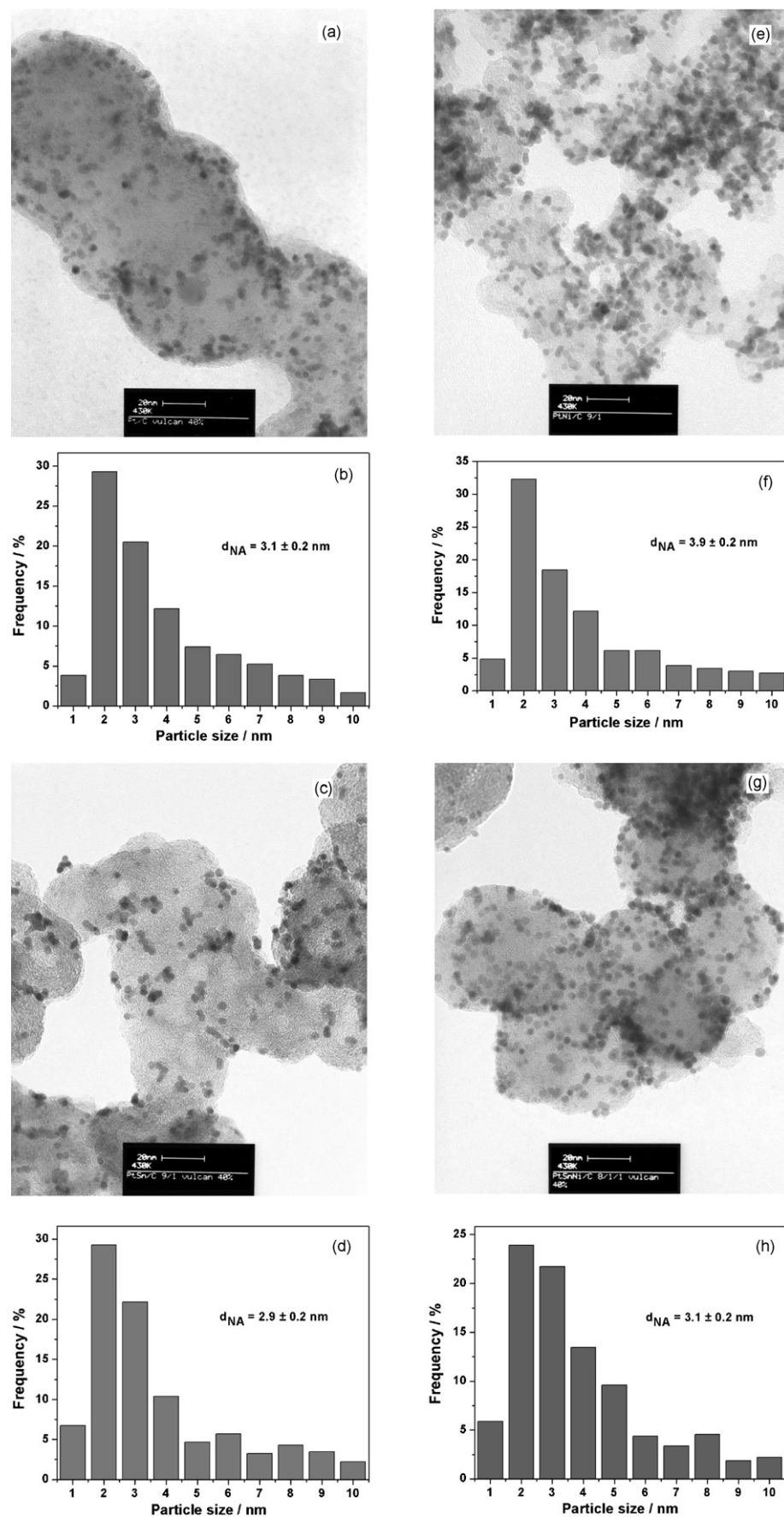


Fig. 4. TEM images and particle size distribution histograms for Pt/C (a, b), Pt₉₀Sn₁₀/C (c, d), Pt₉₀Ni₁₀/C (e, f), and Pt₈₀Sn₁₀Ni₁₀/C (g, h) catalysts.

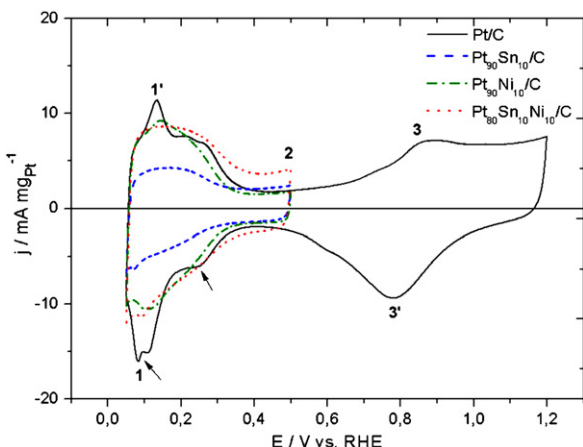


Fig. 5. Cyclic voltammograms of Pt/C (solid line), Pt₉₀Sn₁₀/C (dash line), Pt₉₀Ni₁₀/C (dash-dot line) and Pt₈₀Sn₁₀Ni₁₀/C (dot line) catalysts in 0.1 M HClO₄ with a scan rate of 20 mV s⁻¹.

homogeneity in the composition was obtained with the addition of Ni to Pt₉₀Sn₁₀/C catalyst.

Figs. 2 and 3 showed the XPS spectra of Pt 4f_{7/2} level for Pt/C, Pt₉₀Sn₁₀/C, Pt₈₀Sn₁₀Ni₁₀/C and Sn 3d_{5/2} core level for Pt₉₀Sn₁₀/C and Pt₈₀Sn₁₀Ni₁₀/C catalysts.

In the case of Pt₈₀Sn₁₀Ni₁₀/C catalyst, the Sn 3d_{5/2} signal show only one component with BE of 487.51 eV. This could be ascribed to tin oxide retaining chemisorbed oxygen. It can be also noted that most of the XPS studies reported in the literature data [43] do not allow definition between Sn(II) and Sn(IV) species since both species have a very small difference in the binding energy. In the case of Pt₉₀Sn₁₀/C catalyst, the Sn 3d_{5/2} signal derives of two components: a main one at 487.88 eV corresponding to tin oxide on which oxygen is chemisorbed, and a weaker one at 486.55 eV which would ascribe to the oxidized Sn species or to the formation of Sn(OH)_x species. However, binding energies of the Sn 3d_{5/2} core level somewhat above 486 eV could be assigned to reduced species Sn⁰ (alloyed), reported by some authors [44]. But in line with XRD results, the presence of Sn⁰ (alloyed) species is discarded.

3.3. TEM analysis

The TEM images of catalysts are shown in Fig. 4, together with the obtained averaged value of the particle diameter distribution histograms. As can be seen from the micrographs, all catalysts have a good dispersion on Vulcan XC72 with a size in the same range and follow a log-normal size distribution [45–47]. The average particle size for Pt/C, Pt₉₀Sn₁₀/C, Pt₉₀Ni₁₀/C and Pt₈₀Sn₁₀Ni₁₀/C catalysts were between 3 and 4 nm. The variation of the mean particle size for these catalysts are quite similar in both cases (TEM and XRD), indicating a good particle dispersion without the formation of large particle aggregates. However, the particle size for Pt₉₀Sn₁₀/C catalyst with a mean diameter of 2.9 ± 0.2 nm is much lower than the value of the average crystallite size calculated from XRD analysis (ca. 6.1 nm, see Table 1), which might be attributed to the presence of some regions where metal particle distribution was less uniform than that shown in Fig. 4c.

3.4. Electrochemical active surface area of the catalysts

The cyclic voltammetry (CV) curves of the catalysts are obtained in the supporting electrolyte of 0.1 M HClO₄ and the results are presented in Fig. 5, compared with Pt/C catalyst. The curves stabilized after 10 cycles and no severe changes in the shape or size of the voltammograms are observed during the whole period

Table 4

Catalyst	Q _H /μC	Electrode real surface area (cm ²)	S _{EAS} (m ² g _{Pt} ⁻¹) ^a	Roughness
Pt	780	4.8	49	68
Pt ₉₀ Sn ₁₀ /C	195	1.2	13	17
Pt ₉₀ Ni ₁₀ /C	608	3.8	42	53
Pt ₈₀ Sn ₁₀ Ni ₁₀ /C	425	2.6	33	37

^a The electrochemical active surface area (S_{EAS}) was calculated from Eq. (4).

of measurements for all catalysts. However, in order to avoid dissolution of the non-noble metal in the catalysts, the upper potential limit was set to 0.5 V, except for the Pt/C catalyst.

As shown in Fig. 5, the base CV in 0.1 M HClO₄ of Pt/C presents the characteristic features of polycrystalline Pt electrodes [48,49], regarding the hydrogen adsorption (1) and desorption (1') signals (the hydrogen region), then a potential range free from Faradic processes (double layer region-2), followed by surface oxide formation (3) and oxide reduction (3') currents (the oxygen region). Hydrogen region between 0.05 and 0.35 V, the voltammetric features of the all investigated catalysts are somewhat different because of catalyst's features in this region are influenced by their surface composition.

The characteristic features of the hydrogen adsorption/desorption peaks on the Pt₉₀Sn₁₀/C catalyst are significantly smaller than those on the Pt and Pt-based catalysts. The drastic decrease of H₂ adsorption is also simply explained if one considers that in the bimetallic phase each element retains its chemical bulk properties: platinum metal is well-known to chemisorb hydrogen whereas tin metal does not. Passos et al. [50] found the main effect of tin addition on the chemisorptions of hydrogen on platinum is geometric in nature. According to the authors, any electronic effect plays only a minor role. They also reported preferential coverage of high binding sites on platinum by the tin atoms. Similar results were also reported by Frelink et al. [51] who prepared of Sn onto Pt catalysts and found that Sn was preferentially deposited onto Pt active sites for hydrogen adsorption. On the Pt₉₀Ni₁₀/C catalysts, H adsorption on platinum is suppressed in comparison to Pt/C and the typical Pt peaks are not clearly resolved, possibly originates from blockage of Ni species on Pt atoms at the surface. This phenomenon has also been observed by other researchers for the Pt-M catalysts (M=Ni, Co, Fe, Cr) [52]. In the case of a trimetallic catalyst, the interpretation of these data is not simple due to the overlapping of the different voltammetric behaviours on the basis of the shapes of CV. A gradual decrease of typical Pt features is observed on bimetallic catalysts after modification with Sn.

From the CVs, the electrochemically active surface area (S_{EAS}) is determined by integration of the anodic current corresponding to hydrogen desorption reaction with the correction of double layer region. The S_{EAS} values which can be calculated from Eq. (4):

$$S_{EAS}(\text{m}^2 \text{g}^{-1}) = \frac{Q_H}{210 \times 0.77 \times [\text{Pt}]} \quad (4)$$

where Q_H (μC cm⁻²) represents the charges corresponding to desorption of hydrogen on the Pt surface, [Pt] (mg cm⁻²) is the Pt loading on the electrode surface, 210 μC/real cm² is the charge required to oxidize a monolayer of hydrogen on the Pt surface, 0.77 is the hydrogen monolayer coverage [53]. The roughness of each electrode is calculated by dividing S_{EAS} obtained with the apparent surface area. Estimation of the electrode roughness and S_{EAS} values are shown in Table 4. Based on these values, Pt/C and Pt₉₀Ni₁₀/C were very close to each other, indicating that the activity for ethanol oxidation of these catalysts is near the same. However, for the Pt₉₀Ni₁₀/C prepared here by Bönnemann method, the electrochemically active surface area is 95% higher than Pt₈₀Ni₂₀/C formulations

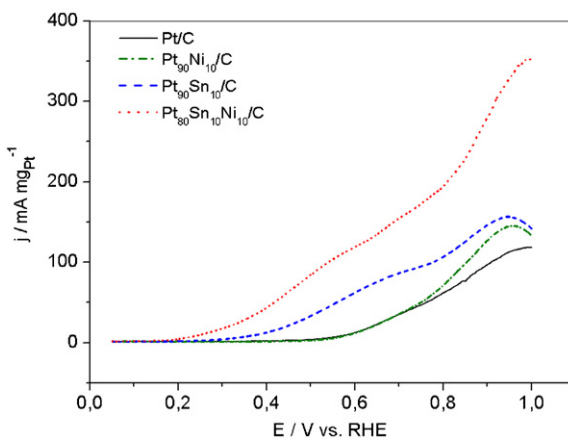


Fig. 6. Linear sweep voltammograms for electrooxidation of 1 M ethanol in 0.1 M $\text{HClO}_4(\text{aq})$ on the Pt/C (solid line), $\text{Pt}_{90}\text{Sn}_{10}/\text{C}$ (dash line), $\text{Pt}_{90}\text{Ni}_{10}/\text{C}$ (dash-dot line) and $\text{Pt}_{80}\text{Sn}_{10}\text{Ni}_{10}/\text{C}$ (dot line) catalysts. Scan rate: 1 mV s^{-1} , at room temperature.

prepared by Pechini method [23]. This may be related to the both lower particle size distribution (ca. 3–4 nm vs. ca. 7–9 nm) and higher degree of alloying.

3.5. Electrochemical activity of the catalysts for ethanol oxidation

The catalytic activities of the carbon-supported Pt/C, $\text{Pt}_{90}\text{Sn}_{10}/\text{C}$, $\text{Pt}_{90}\text{Ni}_{10}/\text{C}$ and $\text{Pt}_{80}\text{Sn}_{10}\text{Ni}_{10}/\text{C}$ catalysts for ethanol electrooxidation are investigated at ambient temperature by linear sweep voltammetry (LSV) at a slow scan rate of 1 mV s^{-1} in 1 M EtOH + 0.1 M $\text{HClO}_4(\text{aq})$ solution (Fig. 6). It is observed that $\text{Pt}_{90}\text{Sn}_{10}/\text{C}$ and $\text{Pt}_{80}\text{Sn}_{10}\text{Ni}_{10}/\text{C}$ catalysts exhibited significantly enhanced catalytic activities for ethanol oxidation relative to Pt and $\text{Pt}_{90}\text{Ni}_{10}/\text{C}$ catalysts in the low potential region of fuel cell. Also, the onset potentials for ethanol oxidation on all of the $\text{Pt}_{90}\text{Sn}_{10}/\text{C}$ and $\text{Pt}_{80}\text{Sn}_{10}\text{Ni}_{10}/\text{C}$ catalysts were significantly lower than that on the Pt catalyst (Table 5). This indicates that the presence of Sn improves the performance of the Pt catalyst. The decrease of the over potential of ethanol oxidation is due to activation of interfacial water molecules forming OH species at less anodic potential than Pt, with the result that completion of the oxidation of ethanol residues, i.e. adsorbed CO leading to CO_2 , and of acetaldehyde to acetic acid [54–57]. It appears that $\text{Pt}_{80}\text{Sn}_{10}\text{Ni}_{10}/\text{C}$ is the electrode material which presents the best activity for ethanol oxidation with an onset potential at 0.17 V and its peak current density is over three times higher than that of $\text{Pt}_{90}\text{Sn}_{10}/\text{C}$ catalyst. The much higher activities of the $\text{Pt}_{80}\text{Sn}_{10}\text{Ni}_{10}/\text{C}$ catalyst for ethanol oxidation relative to $\text{Pt}_{90}\text{Sn}_{10}/\text{C}$ catalyst can be attributed to changes in the platinum lattice due to the addition of Ni and to interaction between platinum and nickel, which could favour C–C bond cleavage, while the CO-intermediates formed during breaking of C–C bond, were removed by tin oxide species.

At low potential, the catalytic activity of Pt/C for ethanol oxidation is only slightly higher than that of $\text{Pt}_{90}\text{Ni}_{10}/\text{C}$ (Table 5). Park

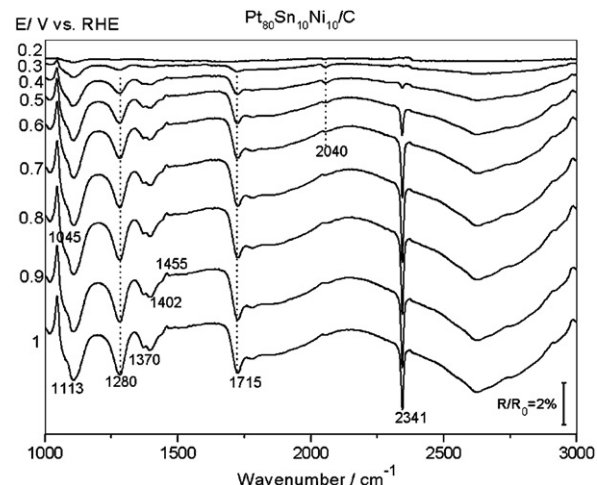


Fig. 7. SPAIR spectra of the species resulting from the adsorption and oxidation of 0.1 M ethanol in 0.1 M HClO_4 on the $\text{Pt}_{80}\text{Sn}_{10}\text{Ni}_{10}/\text{C}$ catalyst at different potentials.

et al. [58], however, found the enhanced activity of $\text{Pt}_m\text{Ni}_n/\text{C}$ (with atomic ratio 1:1) as compared to the Pt/C for methanol oxidation in acid solution, which was interpreted as a decreasing the level of Ni oxide and Ni oxidized states as result of increasing Pt/Ni ratio from 1 to 3 in the $\text{Pt}_m\text{Ni}_n/\text{C}$ catalyst. Thus we also expect that the high Pt/Ni atomic ratio (9:1) in the present study may result in decreasing the amorphous Ni oxides in the catalyst, which could be not detected by XRD, and increasing the level of alloying in the $\text{Pt}_{90}\text{Ni}_{10}/\text{C}$. However, the presence of Pt surface oxides (ca. 44%) in the Pt/C, as evident from the XPS measurements, may play some significant role in providing OH species to remove the adsorbed CO at lower potential than that of $\text{Pt}_{90}\text{Ni}_{10}/\text{C}$ for ethanol oxidation.

3.6. Spectroelectrochemical characterization of the catalyst

Fig. 7 shows the IR reflectance spectra obtained for ethanol oxidation on $\text{Pt}_{80}\text{Sn}_{10}\text{Ni}_{10}/\text{C}$ catalyst. The adsorbed CO_L formation at about 2040 cm^{-1} is observed between 0.2 and 0.6 V vs. RHE and it is totally consumed above 0.7 V vs. RHE. CO_2 appears at ca. 0.5 V vs. RHE according to the band at 2345 cm^{-1} and increases its intensity with the potential. This indicates that there should be other intermediates than adsorbed CO to be further oxidized to CO_2 . Ethanol is oxidized to AA at very low potentials (0.3 V vs. RHE). The feature near 1368 cm^{-1} and 1402 cm^{-1} are associated with the C–H and C–O stretching mode of acetate, respectively. It should be noted that these bands appear after the formation of acetic acid. The vibration C=O of the carbonyl groups of the acetaldehyde or acetic acid (1715 cm^{-1}) appears at around 0.3 V. However, it is perturbed by the water bending mode about 1640 cm^{-1} . The consumption of ethanol begins from 0.3 V in the thin layer and this is observed in the form of positive going bands at 1045 and 1454 cm^{-1} .

3.7. Direct ethanol single cell tests

Fig. 8 shows the polarization and power density curves of DEFCs with Pt/C, $\text{Pt}_{90}\text{Sn}_{10}/\text{C}$ and $\text{Pt}_{80}\text{Sn}_{10}\text{Ni}_{10}/\text{C}$ catalysts as anode ($2 \text{ mg}_{\text{metal}} \text{ cm}^{-2}$, metal loading 40 wt.%), Pt/C E-TEK ($2 \text{ mg}_{\text{metal}} \text{ cm}^{-2}$, metal loading 40 wt.%) catalyst as cathode. The comparison of electrocatalytic activity of catalysts according to the open-circuit voltage and peak power density are also shown in Table 6.

The current density at 0.4 V (where the polarization is mainly affected by activity of the catalyst) for the $\text{Pt}_{80}\text{Sn}_{10}\text{Ni}_{10}/\text{C}$ catalyst was around 80 mA/cm^2 . This corresponds to a 300% increase as compared to the value of ca. 20 mA/cm^2 for the $\text{Pt}_{90}\text{Sn}_{10}/\text{C}$

Table 5
Comparison of mass activity and onset potential for ethanol oxidation reaction (EOR).

Catalyst	Onset potential for EOR ^a (mV vs. RHE)	$J_{400 \text{ mV}}^a$ (mA mg _{Pt} ⁻¹)	$J_{500 \text{ mV}}^a$ (mA mg _{Pt} ⁻¹)
Pt	0.37	2	4.2
$\text{Pt}_{90}\text{Sn}_{10}/\text{C}$	0.21	12.8	33.4
$\text{Pt}_{90}\text{Ni}_{10}/\text{C}$	0.43	1.6	3.3
$\text{Pt}_{80}\text{Sn}_{10}\text{Ni}_{10}/\text{C}$	0.17	43.8	84.5

^a The onset potential and activity data were taken from the LSVs shown in Fig. 6.

Table 6Single-cell DEFCs performances of Pt/C, Pt₉₀Sn₁₀/C and Pt₈₀Sn₁₀Ni₁₀/C as anode catalysts.

Catalyst	Open circuit voltage (mV)	Current density (mA/cm ²)			Maximum power density (mW cm ⁻²)	Normalized maximum power ^a (W g _{Pt} ⁻¹)
		0.3 V	0.4 V	0.5 V		
Pt ₁₀₀	530	13.4	3.8	0.6	6	3
Pt ₉₀ Sn ₁₀ /C	657	37.8	20.3	7.8	12	8
Pt ₈₀ Sn ₁₀ Ni ₁₀ /C ^b	760	107.6	78.2	47.9	33	21
Pt ₈₀ Sn ₁₀ Ni ₁₀ /C ^c	760	159.6	124.9	83.7	47	30

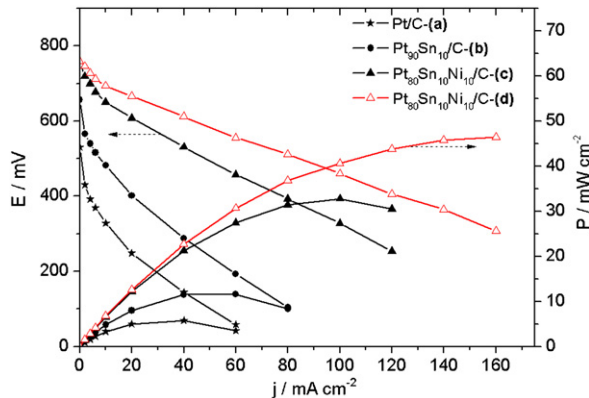
^a The values are determined from the EDX bulk composition (Table 2).^b 1 M.^c 2 M ethanol.

Fig. 8. The polarization and power density curves for a direct ethanol fuel cell using Pt/C, Pt₉₀Sn₁₀/C and Pt₈₀Sn₁₀Ni₁₀/C anode catalysts (2 mg/cm² total metal loading, 40 wt.% catalyst on Vulcan XC-72); cathode catalyst: 2 mg/cm² (40 wt.% Pt/C E-TEK). $T_{cell} = 80^\circ\text{C}$; [EtOH] = 1 M (a, b, c) and 2 M (d); P(EtOH) = 1 bar; P(O₂) = 3 bar; Electrolyte: Nafion® 117 membrane.

catalyst. With Pt₈₀Sn₁₀Ni₁₀/C catalyst the maximum power density was around 33 mW cm⁻² while Pt₉₀Sn₁₀/C catalyst yielded only 11 mW cm⁻². This also indicates that the Pt₈₀Sn₁₀Ni₁₀/C catalyst exhibited 210% higher power density than the Pt₉₀Sn₁₀/C catalyst. The open-circuit voltage (OCV) was also around 0.76 V for Pt₈₀Sn₁₀Ni₁₀/C catalyst. These results demonstrate that the addition of Ni into the Pt₉₀Sn₁₀/C catalyst can promote its ethanol oxidation reaction activity in agreement with half cell studies. The ability of the activation water at low potentials is primarily responsible to significant increase of catalytic activity of these catalysts.

The influence of ethanol concentration (1 M and 2 M) on the DEFCs performance for Pt₈₀Sn₁₀Ni₁₀/C catalyst is also illustrated in Fig. 8 and the results presented in Table 6. The use of higher ethanol concentration (2 M) led to an increase in the current density but no effect on the open circuit voltage. The maximum power density was about 33 mW cm⁻² obtained in the presence of 1 M ethanol whereas the maximum power density was 47 W cm⁻² in the presence of 2 M ethanol which gave rise to an increase about 40%. The single DEFCs performances obtained for the Pt₈₀Sn₁₀Ni₁₀/C (47 mW cm⁻²) catalyst is promising when compared to those obtained with the reported in the literature under the same operating conditions [7,11,12,26,29,59–62]. Recently, however, the comparatively high DEFC performance values reported by Zignani et al. [63] and by De Souza et al. [28,64] but operated at higher temperature than the present study (80 °C vs. 90 °C [63] and 100 °C [28,64]), suggesting the promoting effect of alloyed SnO_x.

4. Conclusions

The main objective of this study was the development of an active Pt–Sn anode catalyst prepared by Bönnemann precursor

method. Pt/C, Pt₉₀Sn₁₀/C, Pt₉₀Ni₁₀/C and Pt₈₀Sn₁₀Ni₁₀/C catalysts activities for ethanol oxidation in acid medium were investigated in terms of cyclic voltammetry and single fuel cell measurements. It was found that the catalytic activity in 1 M EtOH + 0.1 M HClO₄ solution at 0.5 V vs. RHE increases in the following sequence: Pt₈₀Sn₁₀Ni₁₀/C > Pt₉₀Sn₁₀/C > Pt/C > Pt₉₀Ni₁₀/C. The high activity of Pt₈₀Sn₁₀Ni₁₀/C catalyst was also observed on DEFC, which is consistent with the half cell measurements. In situ IR measurements showed that ethanol is favoured to acetic acid (AA) at very low potentials. Besides a high selectivity towards AA formation, Pt₈₀Sn₁₀Ni₁₀/C catalyst exhibited a high yield of CO₂. XPS results revealed that the surface composition of Pt₉₀Sn₁₀/C catalyst is Sn enriched while Pt₈₀Sn₁₀Ni₁₀/C catalyst is Pt-rich. Therefore, the presence of Ni in Pt–Sn that would be effective in reducing non-alloyed SnO_x species and could promote the C–C bond cleavage reaction on its Pt-rich surface at low potentials. On the other hand, the presence of alloyed SnO_x sites in Pt₈₀Sn₁₀Ni₁₀/C can be involved in the polarization of multiple bonds or electron donor groups of substrate molecules, and they can activate CO chemisorbed on the surface providing the necessary OH species for its oxidation, and leading to higher ethanol oxidation efficiency. These observations were correlated with the structure and surface properties of Pt₈₀Sn₁₀Ni₁₀/C catalyst and the result let us to conclude that Pt₈₀Sn₁₀Ni₁₀/C catalyst seems to be an excellent candidate as an anode catalyst in terms of activity for DEFC.

Acknowledgements

This work was carried out under the support of the French Government and framework of a bilateral cooperation programme between Istanbul Technical University (Turkey) and Université de Poitiers (France). The authors wish to thank to Mrs. Suzie Poulin for performing the XPS measurements (Department of Engineering Physics, Ecole Polytechnique de Montréal).

References

- [1] G.A. Camara, R.B. de Lima, T. Iwasita, Journal of Electroanalytical Chemistry 585 (2005) 128–131.
- [2] N. Fujiwara, K.A. Friedrich, U. Stimming, Journal of Electroanalytical Chemistry 472 (1999) 120–125.
- [3] J.P.I. de Souza, D.L. Queiroz, K. Bergamaski, E.R. Gonzalez, F.C. Nart, Journal of Physical Chemistry B106 (2002) 9825–9830.
- [4] F. Vigier, C. Coutanceau, F. Hahn, E.M. Belgsir, C. Lamy, Journal of Electroanalytical Chemistry 563 (2004) 81–89.
- [5] C. Lamy, E.M. Belgsir, J.-M. Léger, Journal of Applied Electrochemistry 31 (2001) 799–809.
- [6] E. Antolini, Journal of Power Sources 170 (2007) 1–12.
- [7] S. Rousseau, C. Coutanceau, C. Lamy, J.-M. Léger, Journal of Power Sources 158 (2006) 18–24.
- [8] E. Antolini, F. Colmati, E.R. Gonzalez, Electrochemistry Communications 9 (2007) 398–404.
- [9] A.O. Neto, R.R. Dias, M.M. Tusi, M. Linardi, E.V. Spinacé, Journal of Power Sources 166 (2007) 87–91.
- [10] E.M. Cunha, J. Ribeiro, K.B. Kokoh, A.R. de Andrade, International Journal of Hydrogen Energy 36 (2011) 11034–11042.

[11] J. Ribeiro, D.M. dos Anjos, K.B. Kokoh, C. Coutanceau, J.-M. Léger, P. Olivi, A.R. de Andrade, G. Tremiliosi-Filho, *Electrochimica Acta* 52 (2007) 6997–7006.

[12] J. Tayal, B. Rawat, S. Basu, *International Journal of Hydrogen Energy* 36 (2011) 14884–14897.

[13] M. Zhu, G. Sun, S. Yan, H. Li, Q. Xin, *Energy and Fuels* 23 (2009) 403–407.

[14] F.E. Teran, D.M. Santos, J. Ribeiro, K.B. Kokoh, *Thin Solid Films* 520 (2012) 5846–5850.

[15] S. Song, C. He, J. Liu, Y. Wang, A. Brouzgou, P. Tsakarous, *Applied Catalysis B119* (2012) 227–233.

[16] F. Colmati, E. Antolini, E.R. Gonzalez, *Journal of Alloys and Compounds* 456 (2008) 264–270.

[17] A. Kowal, M. Li, M. Shao, K. Sasaki, M.B. Vukmirovic, J. Zhang, N.S. Marinkovic, P. Liu, A.I. Frenkel, R.R. Adzic, *Nature Materials* 8 (2009) 325–330.

[18] A. Bonesi, G. Garaventa, W.E. Triaca, A.M. Castro Luna, *International Journal of Hydrogen Energy* 33 (2008) 3499–3501.

[19] E.V. Spinace, M. Linardi, A.O. Neto, *Electrochemistry Communications* 7 (2005) 365–369.

[20] E.V. Spinace, M. Linardi, A.O. Neto, *Materials Letters* 62 (2008) 2099–2102.

[21] A. Bonesi, M.S. Moreno, W.E. Triaca, A.M. Castro Luna, *International Journal of Hydrogen Energy* 35 (2010) 5999–6004.

[22] E. Ribaneira, B.A. Hayos, *Journal of Power Sources* 180 (2008) 238–242.

[23] T.S. Almeida, K.B. Kokoh, A.R. de Andrade, *International Journal of Hydrogen Energy* 36 (2011) 3803–3810.

[24] P. dos Santos Correa, E.L. da Silva, R.F. Da Silva, C. Radtke, B. Moreno, E. Chiarro, C. de Fraga Malfatti, *International Journal of Hydrogen Energy* 37 (2012) 9314–9323.

[25] E. Lee, A. Murthy, A. Manthiram, *Electrochimica Acta* 56 (2011) 1611–1618.

[26] J. Ribeiro, D.M. dos Anjos, J.-M. Léger, F. Hahn, P. Olivi, A.R. de Andrade, G. Tremiliosi-Filho, K.B. Kokoh, *Journal of Applied Electrochemistry* 38 (2008) 653–662.

[27] F. Wang, Y. Zheng, Y. Guo, *Fuel Cells* 10 (2010) 1100–1107.

[28] R.F.B. De Souza, L.S. Parreira, J.C.M. Silva, F.C. Simoes, M.L. Calegaro, M.J. Giz, G.A. Camara, A.O. Neto, M.C. Santos, *International Journal of Hydrogen Energy* 36 (2011) 11519–11527.

[29] J. Tayal, B. Rawat, S. Basu, *International Journal of Hydrogen Energy* 37 (2012) 4597–4605.

[30] H. Bönnemann, W. Brijoux, R. Brinkmann, E. Dinjus, T. Joussen, B. Korall, *Angewandte Chemie (International ed. in English)* 30 (1991) 1312–1314.

[31] H. Bönnemann, W. Brijoux, R. Brinkmann, R. Fretzen, T. Joussen, R. Köppler, B. Korall, P. Neiteler, J. Richter, *Journal of Molecular Catalysis* 86 (1996) 129–177.

[32] H. Bönnemann, G. Braun, W. Brijoux, R. Brinkmann, A. Schulze Tilling, K. Seevogel, K. Siepen, *Journal of Organometallic Chemistry* 520 (1996) 143–162.

[33] H. Bönnemann, W. Brijoux, *Active Metals: Preparation, Characterization, Applications*, VCH, Weinheim, Germany, 1995, pp. 339–378.

[34] H. Bönnemann, R.M. Richards, *European Journal of Inorganic Chemistry* 2001 (2001) 2455–2480.

[35] H. Bönnemann, R. Brinkmann, P. Britz, U. Endruschat, R. Mörtel, U.A. Paulus, G.J. Feldmeyer, T.J. Schmidt, H.A. Gasteiger, R.J. Behm, *Journal of New Materials for Electrochemical Systems* 3 (2000) 199–206.

[36] V. Radmilovic, H.A. Gasteiger, P.N. Ross, *Journal of Catalysis* 154 (1995) 98–106.

[37] C.D. Wagner, L.E. Davis, R.H. Raymond, *Surface and Interface Analysis* 3 (1981) 211–225.

[38] D.A. Shirley, *Physical Review B-Condensed Matter* 5 (1972) 4709–4712.

[39] A.K. Shukla, M.K. Ravikumar, A. Roy, S.R. Baraman, D.D. Sarma, A. Arico, V. Antonucci, L. Pino, N. Giordano, *Journal of the Electrochemical Society* 141 (1994) 1517–1522.

[40] A.K. Shukla, A. Arico, K.M. Ell-Kathib, H. Kim, P.L. Antonucci, *Applied Surface Science* 137 (1999) 20–29.

[41] V.I. Kuznetsov, A.S. Belyi, E.N. Yurchenko, M.D. Smolikov, M.T. Protasova, E.V. Zatolokina, V.K. Duplyakin, *Journal of Catalysis* 99 (1986) 159–170.

[42] D. Briggs, M.P. Seah, *Practical Surface Analysis*, Wiley, New York, 1990.

[43] C.L. Lau, G.K. Wertheim, *Journal of Vacuum Science & Technology* 15 (1978) 622–624.

[44] M.M. Schubert, M.J. Kahlich, G. Feldmeyer, M. Hüttner, S. Hackenberg, H.A. Gasteiger, R.J. Behm, *Physical Chemistry Chemical Physics* 3 (2001) 1123–1131.

[45] C.G. Granqvist, R.A. Buhrman, *Journal of Catalysis* 42 (1976) 477–479.

[46] C.G. Granqvist, R.A. Buhrman, *Journal of Applied Physics* 47 (1976) 2200–2222.

[47] P. Ehrburger, P.R. Walker Jr., *Journal of Catalysis* 55 (1978) 63–70.

[48] R. Woods, in: A.J. Bard (Ed.), *Electroanalytical Chemistry*, Vol. 9, Marcel Dekker, New York, 1976, pp. 2–162.

[49] D.A.J. Rand, R. Woods, *Journal of Electroanalytical Chemistry* 36 (1972) 57–69.

[50] F.B. Passos, M. Schmal, M.A. Vannice, *Journal of Catalysis* 160 (1996) 106–117.

[51] T. Frelink, W. Visscher, J.A.R. van Veen, *Electrochimica Acta* 39 (1994) 1871–1875.

[52] C. Roth, N. Benker, T. Buhrmester, M. Mazurek, M. Loster, H. Fuess, D.C. Koningsberger, D.E. Ramaker, *Journal of the American Chemical Society* 127 (2005) 14607–14615.

[53] T. Biegler, D.A.J. Rand, R. Woods, *Journal of Electroanalytical Chemistry* 29 (1971) 269–277.

[54] C. Lamy, S. Rousseau, C. Coutanceau, F. Hahn, C. Lamy, *Electrochimica Acta* 49 (2004) 3901–3908.

[55] J.-M. Léger, S. Rousseau, C. Coutanceau, F. Hahn, C. Lamy, *Electrochimica Acta* 50 (2005) 5118–5125.

[56] F.L.S. Purgato, P. Olivi, J.-M. Léger, A.R. Andrade, G. Tremiliosi-Filho, E.R. Gonzalez, C. Lamy, K.B. Kokoh, *Journal of Electroanalytical Chemistry* 628 (2009) 81–89.

[57] F.C. Simoes, D.M. dos Anjos, F. Vigier, J.-M. Léger, F. Hahn, C. Coutanceau, E.R. Gonzalez, G. Tremiliosi-Filho, A.R. de Andrade, P. Olivi, K.B. Kokoh, *Journal of Power Sources* 167 (2007) 1–10.

[58] K-W. Park, J-H. Choi, B-K. Kwon, S-A. Lee, Y-E. Sung, H-Y. Ha, S-A. Hong, H. Kim, A. Wieckowski, *Journal of Physical Chemistry B106* (2002) 1869–1877.

[59] F. Colmati, E. Antolini, E.R. Gonzalez, *Journal of the Electrochemical Society* 154 (2007) B39–B47.

[60] F. Colmati, E. Antolini, E.R. Gonzalez, *Applied Catalysis B73* (2007) 106–115.

[61] F.L.S. Purgato, S. Pronier, P. Olivi, A.R. de Andrade, J.M. Léger, G. Tremiliosi-Filho, K.B. Kokoh, *Journal of Power Sources* 198 (2012) 95–99.

[62] T.S. Almeida, L.M. Palma, P.H. Leonello, C. Morais, K.B. Kokoh, A.R. De Andrade, *Journal of Power Sources* 215 (2012) 53–62.

[63] S.C. Zignani, V. Baglio, J.J. Linares, G. Monforte, E.R. Gonzalez, A.S. Aricò, *Electrochimica Acta* 70 (2012) 255–265.

[64] R.F.B. De Souza, L.S. Parreira, D.C. Rascio, J.C.M. Silva, E. Teixeira-Neto, M.L. Calegaro, E.V. Spinace, A.O. Neto, M.C. Santos, *Journal of Power Sources* 195 (2010) 1589–1593.